INSTITUTE OF PHYSICS PUBLISHING JOURNAL OF PHYSICS B: ATOMIC, MOLECULAR AND OPTICAL PHYSICS

J. Phys. B: At. Mol. Opt. Phys. **36** (2003) 3203–3218 PII: S0953-4075(03)59199-4

Electron-impact cross sections of atomic oxygen

P V Johnson[1], I Kanik[1], D E Shemansky[2] and X Liu[2]

[1] Jet Propulsion Laboratory, California Institute of Technology, 4800 Oak Grove Drive, Pasadena, CA 91109, USA
[2] Department of Aerospace and Mechanical Engineering, University of Southern California, Los Angeles, CA 90089, USA

Received 29 January 2003
Published 11 July 2003
Online at stacks.iop.org/JPhysB/36/3203

Abstract

We report electron-impact-induced emission cross sections for the $2p^4\ ^3P$–$3s\ ^3S^o$ (130.4 nm), $2p^4\ ^3P$–$3d\ ^3D^o$ (102.7 nm), $2p^4\ ^3P$–$3s'\ ^3D^o$ (98.9 nm) and $2p^4\ ^3P$–$3s''\ ^3P^o$ (87.8 nm) transitions of atomic oxygen. Measurements were made using a magnetically confined electron beam in collision with atomic oxygen produced by an extended microwave discharge source in a crossed-beam arrangement. A 0.2 m vacuum ultraviolet diffraction spectrometer was used to record the emission. The absolute excitation functions of these transitions were determined by normalizing to the O I (130.4 nm) cross section produced by dissociative excitation of O_2 at 100 eV impact energy (Noren *et al* 2001a *Geophys. Res. Lett.* **28** 1379). A 60-state model of the O I electron reaction structure has been used to extract the excitation cross sections from the experimental measurements. The model process establishes analytic collision strengths to the asymptotic limit.

1. Introduction

Electron-impact-induced emission from atomic oxygen in the vacuum ultraviolet (VUV) is an important feature in astrophysical sources and, for this reason, an accurate model will allow consistent diagnostic analyses of the oxygen-bearing atmospheric and nebular environments. In our inaugural study of electron-impact excitation of atomic oxygen (Kanik *et al* 2001), electron scattering cross sections, both differential and integral, for direct excitation of the $2p^4\ ^3P$–$3s\ ^3S^o$ (130.4 nm), $2p^4\ ^3P$–$3d\ ^3D^o$ (102.7 nm), $2p^4\ ^3P$–$3s'\ ^3D^o$ (98.9 nm) and $2p^4\ ^3P$–$3s''\ ^3P^o$ (87.8 nm) transitions at 30, 50 and 100 eV electron-impact energies were presented. Noren *et al* (2001b) have measured the electron-induced emission cross section of the $3s\ ^3S^o$ state, allowing a comparison with the direct excitation measurements by Kanik *et al* (2001). The 130.4 nm excitation function has been remeasured with improved procedures and apparatus, and the results presented here supersede the Noren *et al* (2001b) results. The reader is referred to Kanik *et al* (2001) for a general introduction and survey of previous atomic oxygen investigations.

0953-4075/03/153203+16$30.00

As discussed in Noren *et al* (2001b), electron-impact-induced emission measurements provide complementary information to electron-impact direct excitation measurements and, in principle, allow one to determine the magnitude of the cascade transitions. Direct excitation cross sections, such as those presented in Kanik *et al* (2001), provide values of the direct excitation of an atomic state from the ground state while cross sections for emission to the ground state, as presented in both Noren *et al* (2001b) and the present work, provide the accumulated excitation of an atomic level through both direct excitation and cascade from higher-lying levels.

Electron-impact-induced emission cross sections of the 130.4, 102.7, 98.9 and 87.8 nm lines of atomic oxygen have been investigated in the past. Wang and McConkey (1992) provided comparisons of the existing data for these lines that included their own work as well as the results of Zipf and Erdman (1985) and Zipf and Kao (1986). Wang and McConkey (1992) have demonstrated that there is little consensus among the previous measurements in either shape or magnitude. We therefore undertook the task of measuring the 130.4, 102.7, 98.9 and 87.8 nm emission cross sections from atomic oxygen in order to establish more accurate values and provide a basis for construction of a viable full model of the O I electron reaction structure. A fine structure model of O I composed of 60 electronic states has been constructed with the present and other available collision strength data (Shemansky and Liu 2003).

2. Experimental apparatus and procedures

The experimental apparatus and experimental techniques employed in the electron-impact-induced emission cross section measurements have been described in detail by Noren *et al* (2001b). Only a brief outline of the changes in the apparatus and differences in procedure will be presented. The reader is referred to Noren *et al* (2001b) for further details.

In the present experiment, a single electron gun consisting of three electrostatic acceleration and focusing elements, combined with two solenoids, was employed over the entire energy range investigated. This differed from the work of Noren *et al* (2001b) where a purely electrostatic gun was employed at energies higher than 30 eV to avoid trapping of secondary electrons by the collimating magnetic field. In the present work, this use of the 'electrostatic gun' was deemed unnecessary. We found that it was possible to avoid such 'trapping effects' through careful tuning of the 'magnetic gun'. This was determined as follows. After tuning the gun (i.e. adjusting electrostatic potentials and solenoid currents), an O I (130.4 nm) excitation function was measured for dissociative excitation of O_2. The shape of the excitation function was then compared with the known dissociative excitation function for O I (130.4 nm) of Kanik *et al* (2003). If a discrepancy in the shape function was observed (especially at high energies, where magnetically trapped secondary electrons distort the shape of the excitation function), the gun tuning was adjusted. This procedure was repeated until no evidence of trapped secondary electrons could be observed.

It was estimated that the electron beam produced by the gun was approximately 1 mm in radius at the interaction region while the target gas beam was of the order of 2 mm in radius. No lenses were used to collect photons into the spectrometer. Therefore, the spectrometer's field of view was determined solely by the experimental geometry and was such as to include the entire overlap region of the electron and gas beams. Total electron beam current was typically of the order of 65 μA. However, there was some variation in beam current over the range of impact energies studied, particularly at near threshold energies. Therefore, the emission signal, as in Noren *et al* (2001b), was collected as a function of integrated electron beam current (measured on a Faraday cup).

In our previous atomic oxygen work (Kanik *et al* 2001, Noren *et al* 2001b), the microwave discharge source was fed with a mixture of O_2 and a N_2 buffer gas where the presence of the

buffer gas tended to 'enhance' the atomic oxygen production of the source. However, a 100% O_2 feed was used in the present experiments in order to avoid contamination by N I and N_2 lines (Ajello *et al* 1989) located in the vicinity of the O I features being investigated. Further discussion on the use of a N_2 buffer gas will be given.

Subsequent to the measurements by Noren *et al* (2001b), two significant changes were made to the UV spectrometer system:

(1) a diffraction grating coated with SiC was installed in the spectrometer in order to improve reflectance in the extreme ultraviolet (EUV: 40–135 nm) where the emission features investigated in the present work are found;
(2) a new photomultiplier tube was installed which provided a vastly improved signal-to-noise ratio in the far ultraviolet (FUV: 135–300 nm).

A CsI coated channeltron served as the detector for the bulk of the measurements in the EUV.

As in our previous work, determination of the fraction of O_2 molecules dissociated in the source and that which remained dissociated in the collision region (i.e. the dissociation fraction, D) was required for analysis. As in Noren *et al* (2001b), this was accomplished by examining the emission signals, $S_{O_2^+}$, of the second negative band system of O_2^+ with the discharge-on and -off which are directly proportional to the number of O_2 molecules in the beam, i.e.

$$D = 1 - \frac{S^{\mathrm{on}}_{O_2^+}}{S^{\mathrm{off}}_{O_2^+}}. \tag{1}$$

By measuring the O_2^+ signal with the spectrometer tuned to 236.9 nm, at a resolution of 3 nm full width at half-maximum (FWHM), the maximum amount of signal was collected while avoiding possible 'contamination' from the O I (115.2 nm) emission line in the second order. By keeping the conditions in the source constant (gas pressure, tuning of the microwave cavity), we were able to maintain a stable dissociation fraction throughout the entire experiment. These conditions corresponded to a dissociation fraction of 0.22.

As in Noren *et al* (2001b), the present measurements suffered from a complication arising due to a significant presence of O_2 in the target beam. This meant that, when measuring the signal from an atomic oxygen emission line at a given wavelength, λ, and impact energy, E_0, there was also a contribution to the O I (λ) signal through dissociative excitation of O_2 by electron impact. Therefore, measurements were made with both the discharge on, $S^{\lambda}_{O+O_2}$, and off, $S^{\lambda}_{O_2}$, which allowed for the isolation of the atomic oxygen signal, S^{λ}_{O}, according to the following relation:

$$S^{\lambda}_{O}(E_0) = S^{\lambda}_{O+O_2}(E_0) - (1 - D)S^{\lambda}_{O_2}(E_0). \tag{2}$$

Figure 1 shows a spectrum of the atomic features taken using a 100% O_2 feed and calculated using equation (2) (spectral features are identified in table 1). The spectrum has been calibrated for the wavelength dependence of the spectrometer/detection system by means of an electron-impact-induced emission spectrum of H_2. The calibration procedure has been described in detail by Liu *et al* (1995), Abgrall *et al* (1997) and Jonin *et al* (2000). A refined model which includes the $B''\,{}^1\Sigma_u^+$–$X\,{}^1\Sigma_g^+$ and $D'\,{}^1\Sigma_u^+$–$X\,{}^1\Sigma_g^+$ band systems (Abgrall *et al* 2003) has been used for the calibration.

Relative cross section data were obtained as in Noren *et al* (2001b), resulting in two relative atomic excitation functions for each measured transition: one at low-impact energies and one at high-impact energies. Apart from the lack of N_2 buffer gas in the source and the fact that a single electron gun was employed in the present measurements, the only deviation from the

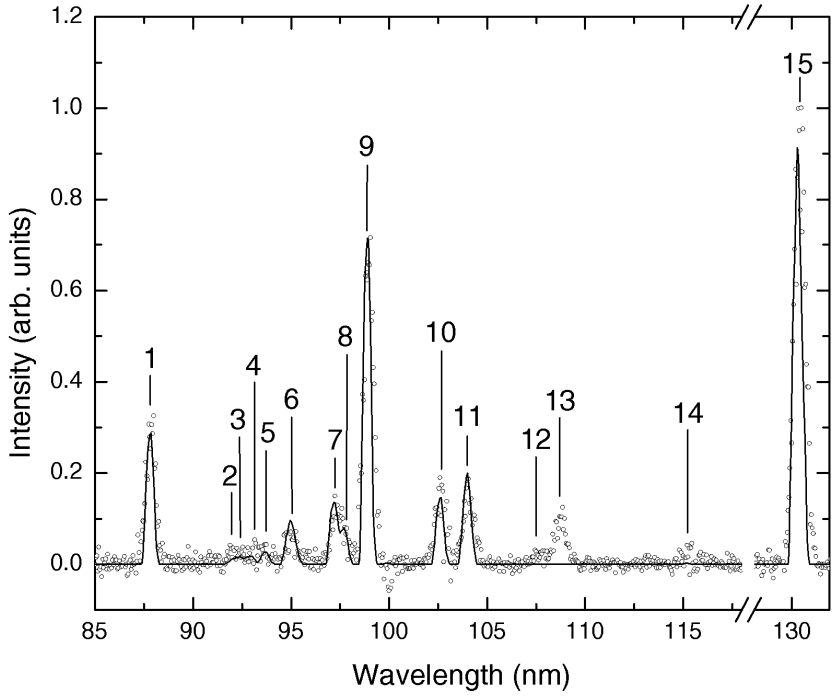

Figure 1. Calibrated electron-impact-induced emission spectrum of atomic oxygen at 100 eV impact energy (open circles) derived from discharge-on and -off spectra (measured with 100% O_2 feeding discharge source) according to equation (2). The model fit to the 100 eV spectrum is also shown (full curve). Features are labelled in the figure and identified in table 1. Note the presence of the O II emission lines (features 12 and 13), which appear in the spectra due to the lack of quenching by a N_2 buffer gas.

procedure described in Noren *et al* (2001b) was the limit imposed on the high and low energy regions. In the present work, 'low-energy' data were taken from 5 eV (below all thresholds) to 205 eV, in 1 eV increments while 'high-energy' data were collected at 100, 200, 300, 400, 500, 750 and 1000 eV. With the exception of the dissociation fraction measurements, all data were taken with the entrance and exit slits of the spectrometer adjusted to give a resolution of approximately 0.5 nm FWHM.

As previously mentioned, the dissociation fraction was observed to be constant during the course of the measurements and was essentially equivalent to that obtained in Noren *et al* (2001b), although the present data were taken with pure O_2 in the source while the measurements by Noren *et al* (2001b) used a 90% O_2/10% N_2 mixture. However, the ratio, R, of 130.4 nm signal under discharge-on and -off conditions, i.e.

$$R = \frac{S^{130.4}_{O+O_2}(E_0)}{S^{130.4}_{O_2}(E_0)}, \tag{3}$$

was substantially different in the present experiment compared to the raw Noren *et al* (2001b) data. In order to understand this apparent paradox, one must keep in mind that the method for determining the dissociation fraction does not measure atomic oxygen density directly, but instead measures the loss of O_2 from the beam as a result of dissociation in the microwave discharge source. In examining this issue, R (equation (3)) was measured at 100 eV using a series of N_2 concentrations ranging from 0 to 80% (balance O_2; all other conditions kept

Table 1. Identification of features observed in the emission spectrum of figure 1.

Feature no	Species	Transition(s)[a]	Observed peak (nm)
1	O I	$2s^2 2p^4\ ^3P–2s^2 2p^3(^2P^o)3s\ ^3P^o$	87.8
2	O I	$2s^2 2p^4\ ^3P–2s^2 2p^3(^4S^o)10d\ ^3D^o$	92.0
		$2s^2 2p^4\ ^3P–2s^2 2p^3(^4S^o)11s\ ^3S^o$	
3	O I	$2s^2 2p^4\ ^3P–2s^2 2p^3(^4S^o)9d\ ^3D^o$	92.3
		$2s^2 2p^4\ ^3P–2s^2 2p^3(^4S^o)10s\ ^3S^o$	
4	O I	$2s^2 2p^4\ ^3P–2s^2 2p^3(^4S^o)7d\ ^3D^o$	93.0
		$2s^2 2p^4\ ^3P–2s^2 2p^3(^4S^o)8s\ ^3S^o$	
5	O I	$2s^2 2p^4\ ^3P–2s^2 2p^3(^4S^o)6d\ ^3D^o$	93.7
6	O I	$2s^2 2p^4\ ^3P–2s^2 2p^3(^4S^o)5d\ ^3D^o$	95.0
		$2s^2 2p^4\ ^3P–2s^2 2p^3(^4S^o)6s\ ^3S^o$	
7	O I	$2s^2 2p^4\ ^3P–2s^2 2p^3(^4S^o)4d\ ^3D^o$	97.3
8	O I	$2s^2 2p^4\ ^3P–2s^2 2p^3(^4S^o)5s\ ^3S^o$	97.7
9	O I	$2s^2 2p^4\ ^3P–2s^2 2p^3(^2D^o)3s\ ^3D^o$	98.9
10	O I	$2s^2 2p^4\ ^3P–2s^2 2p^3(^4S^o)3d\ ^3D^o$	102.7
11	O I	$2s^2 2p^4\ ^3P–2s^2 2p^3(^4S^o)4s\ ^3S^o$	104.0
12	O II	$2s^2 2p^3\ ^2D^o–2s2p^4\ ^4P$	107.5
13	O II	$2s2p^4\ ^4P–2s^2 2p^2(^3P)3p\ ^4S^o$	108.7
14	O I	$2s^2 2p^4\ ^1D–2s^2 2p^3(^2D^o)3s\ ^1D^o$	115.2
15	O I	$2s^2 2p^4\ ^3P–2s^2 2p^3(^4S^o)3s\ ^3S^o$	130.4

[a] Designations taken from the NIST Atomic Spectra Database.

constant). These tests showed that, within experimental uncertainty, R was constant for N_2 concentrations between 5 and 80%. Moreover, the R values determined for non-zero N_2 concentrations were approximately 50% larger than the pure O_2 R value. Since the atomic oxygen cross section is three to four times that of dissociative excitation (Noren *et al* 2001b, Kanik *et al* 2003), these observations indicate that the use of a N_2 buffer gas effectively increases the production of atomic O. As stated earlier, this occurs without visibly affecting the dissociation fraction of the source. In other words, the percentage of dissociation products that emerge from the source as neutral ground state oxygen atoms increases when a N_2 buffer gas is added. Therefore, it was concluded that the dissociation in the source is essentially determined by the source pressure and microwave power, while the presence of N_2 in the gas line serves to catalyze the 'deactivation' of non-neutral ground state oxygen species (i.e. metastable and ion species; see figure 1). Furthermore, one can conclude that the observed effect saturates at low N_2 concentration. Examination of electron energy-loss spectra from the study by Kanik *et al* (2001), where only direct excitation processes are visible, reveals no evidence of O_2 dissociation products other than ground state atomic oxygen (see the discussion in Kanik *et al* 2001). Since these data were taken using a nearly identical discharge source with a 95% O_2/5% N_2 feed, one can conclude that, even with a N_2 concentration of 5%, no significant populations of metastable atomic oxygen, or oxygen ions, emerge from the source. Therefore, we argue that, by using a 90% O_2/10% N_2 feed, one can make a direct link between the dissociation fraction and the concentration of atomic oxygen in the beam. Specifically, we argue that, under these conditions, two neutral ground-state oxygen atoms are produced for every O_2 molecule that remains dissociated at the interaction region (Kanik *et al* 2001, Noren *et al* 2001b).

An important point should be clarified regarding the preceding discussion and the separation of signals resulting from electron impact on atomic oxygen and those resulting from dissociative excitation of O_2 (equation (2)). The relative excitation function measurements

were carried out with 100% O_2 feeding the source. As discussed above, the measured dissociation fraction does not relate directly to the amount of atomic oxygen found in the target beam. However, this is not required for equation (2) to remain valid. The factor $(1 - D)$, found in equation (2) scales the discharge-off signal, which is due purely to dissociative excitation, to the level of dissociative excitation found under discharge-on conditions by providing the ratio of O_2 discharge-on to discharge-off number densities. This is exactly what the current D measurement procedure provides. Therefore, equation (2) correctly accounts for the O_2 dissociative excitation component found in the discharge-on signal in spite of the fact that 100% O_2 was used in the source.

3. Data analysis

3.1. Relative excitation functions

As described above, two relative excitation function data sets were collected for each emission feature examined. The background was determined for the low-energy data sets by taking an average of the 'pre-threshold' channels. This background was subtracted from each channel of the data set. The impact energy was calibrated to the appropriate threshold energy. Discharge-on measurements contain O I emission resulting from populating the parent levels through direct electron-impact excitation, dissociative excitation of O_2 and through cascade from higher levels excited through either of these mechanisms. Since direct excitation is the most energetically efficient channel, the discharge-on thresholds are given by the energies of the appropriate parent levels (9.51, 12.08, 12.54 and 14.11 eV for the 130.4, 102.7, 98.9 and 87.8 nm lines, respectively). However, the discharge-off excitation functions are purely a result of dissociative excitation. Therefore, these thresholds are given by that of the parent line plus the dissociation energy of O_2, namely 5.12 eV (Huber and Herzberg 1979). Typically, the calibrated impact energies differed from the nominal impact energies by 1 eV or less.

The background was determined directly for each high-energy data point by measuring signals at the appropriate wavelength with the cathode potential at ground. This eliminated all collisionally induced signals (i.e. no electron beam) while having no effect on any potential sources of background signal (i.e. electron gun filament). After subtraction of the background, no energy calibration was performed on the high-energy data. As discussed in the preceding paragraph, the calibrated impact energy of the system is typically less than 1 eV from the nominal energy. Therefore, at impact energies in the 100–1000 eV range, the error was insignificant.

In order to produce a single relative excitation function for each line extending from threshold to 1000 eV, corresponding 'high-' and 'low-energy' data sets had to be normalized to one another. This was done by fitting a function to the low energy data sets over the 80–200 eV range. The scaling factors required to bring the 100 eV values produced by the fit to the 100 eV values of the corresponding high-energy data sets were determined. These scaling factors were then applied to each point in the appropriate low-energy data sets, producing smooth relative excitation functions from threshold to 1000 eV for each measured transition. The overlap between 100 and 200 eV in the high- and low-energy data sets was used as a cross-check of the continuity between the low- and high-energy data sets.

3.2. Normalization

The relationship between the electron-impact emission cross section, σ, at a particular wavelength, λ, and impact energy, E_0, for a given target species, a, to the measured signal, S, appropriate to the current experimental arrangement can be written as

$$\sigma_a^{\lambda}(E_0) = \frac{C(1 - p_\lambda/3)\gamma_\lambda S_a^{\lambda}(E_0)}{n_a} \tag{4}$$

(Noren *et al* 2001b), where p_λ is the polarization of the emitted radiation, n_a is the number density of the target species, γ_λ is the relative sensitivity of the detector at a given wavelength, λ, and C represents constant multiplicative factors such as electron beam current, path length through the target, etc. Therefore, any two signals (from species a and A at wavelengths λ and Λ, respectively) measured under equivalent experimental conditions (electron current, source pressure and impact energy) are related through the following expression:

$$\sigma_a^{\lambda}(E_0) = \frac{n_A}{n_a}\frac{(1 - p_\lambda/3)}{(1 - p_\Lambda/3)}\frac{\gamma_\lambda}{\gamma_\Lambda}\frac{S_a^{\lambda}(E_0)}{S_A^{\Lambda}(E_0)}\sigma_A^{\Lambda}(E_0). \tag{5}$$

As in Noren *et al* (2001b), the 130.4 nm excitation function was normalized to a known cross section for the O I (130.4 nm) emission through the dissociative excitation of O_2. As seen from equation (5), this requires detailed knowledge of the O and O_2 number densities in discharge-on and -off measurements, n_O^{on} and $n_{O_2}^{off}$, respectively. Noren *et al* (2001b) give the ratio of these densities in terms of the dissociation fraction as

$$\frac{n_{O_2}^{off}}{n_O^{on}} = \frac{1}{\sqrt{2}D}. \tag{6}$$

In deriving this relationship (Kanik *et al* 2001, Noren *et al* 2001b) it is assumed that there are two O atoms delivered to the interaction region for every O_2 molecule that remains dissociated at the interaction region. As discussed previously, this is not the case when the discharge source was fed with 100% O_2. Therefore, in order to normalize the 130.4 nm excitation function, a measurement of the 130.4 nm signal was taken at 100 eV using a 90% O_2/10% N_2 mixture under discharge-on and -off conditions. Since equation (6) is valid under these conditions, this measurement enabled the determination of the absolute 130.4 nm atomic oxygen cross section at 100 eV. Given that the polarization of O I (130.4 nm) radiation is identically zero (Noren *et al* 2001b), the absolute cross section for electron-impact-induced emission of 130.4 nm radiation from atomic oxygen at 100 eV impact energy was determined according to the following relation:

$$\sigma_O^{130.4} = \frac{1}{\sqrt{2}D}\frac{S_{O+O_2}^{130.4} - (1 - D)S_{O_2}^{130.4}}{S_{O_2}^{130.4}}\sigma_{O_2}^{130.4} \tag{7}$$

where $\sigma_{O_2}^{130.4}$ (100 eV) was given by Noren *et al* (2001a) as 2.83×10^{-18} cm^2. Note that, since the two signals are at the same wavelength, the ratio of the γ's is equal to unity. The 130.4 nm atomic oxygen excitation function was then put on the absolute scale by normalizing to the 100 eV value of $\sigma_O^{130.4}$ as determined by equation (7).

The excitation functions of the remaining transitions under investigation were also normalized to the 100 eV 130.4 nm cross section. In order to do this, a measurement of relative atomic oxygen line intensities at 100 eV impact energy using 100% O_2 in the source was required. This was performed by tuning the spectrometer to a given emission line with the discharge-on and collecting data until acceptable statistics were achieved. This process was repeated for each measured transition, the discharge was turned off and the process was repeated again. The background was determined for both discharge-on and -off conditions by collecting signals at each measured wavelength with the cathode potential set at 0 V. After proper scaling for data acquisition times, relative atomic oxygen intensities were determined for each line from the respective discharge-on and -off measurements according to equation (2). It should be noted that the relative atomic oxygen intensities determined by this procedure are in excellent agreement with the relative intensities found by integrating features in the atomic

oxygen spectrum shown in figure 1. Absolute 100 eV cross sections for the 102.7, 98.9 and 87.8 nm lines (λ) were then determined by normalizing to their previously determined 130.4 nm counterpart by means of the following:

$$\sigma_{\mathrm{O}}^{\lambda} = \frac{\gamma_{\lambda}}{\gamma_{130.4}} \frac{S_{\mathrm{O}}^{\lambda}}{S_{\mathrm{O}}^{130.4}} \sigma_{A}^{130.4}. \tag{8}$$

Note that, since all of the signals involved in this expression result from electron collisions with atomic oxygen, the ratio of n's in equation (5) is equal to unity. Furthermore, in writing equation (8), the polarizations of the 102.7, 98.9 and 87.8 nm lines are taken to be zero. This is not strictly true. However, at high energies (100 eV is ~10 times threshold for all these transitions), the polarization is expected to be small (Heddle 1979). Even polarizations as high as 5% would have a less than 2% effect on the overall normalization of the cross sections in question. Furthermore, if any of these lines were, in fact, significantly polarized, one would see altered shapes in the low energy regions of the excitation functions where the line polarizations will be largest. This is not in evidence. The values for the relative sensitivity of the spectrometer and detector system were determined based on a measured H_2 electron-impact-induced emission spectra according to procedures described in detail elsewhere (Liu *et al* 1995, Abgrall *et al* 1997, Jonin *et al* 2000). Once absolute values for the 102.7, 98.9 and 87.8 nm cross sections were determined at 100 eV, the corresponding relative excitation functions were placed on an absolute scale.

3.3. Experimental uncertainties

The uncertainties associated with the experimental results have a variety of sources. First and foremost among these was the uncertainty in the primary calibration standard; namely the 100 eV cross section for O I (130.4 nm) emission through dissociative excitation of O_2. The value of the cross section was given by Noren *et al* (2001a) with a quoted uncertainty of 22%.

The uncertainty in the determination of the dissociation fraction was also a major contribution. An estimate in the uncertainty of the dissociation fraction was made based on how the 'shape' of the relative 130.4 nm excitation function changed as D was allowed to vary about the experimentally determined value. The modified Born approximation model (Shemansky *et al* 1985a, 1985b) is expected to do well in predicting the shape of optically allowed transitions such as the $2p^4\ ^3P$–$3s\ ^3S^o$ (130.4 nm) transition in atomic oxygen. The asymptotic shape was used as a guide toward the correct shape function. It was found that varying D by more than 10% resulted in obvious deviations from the shape suggested by the model. Before the dissociative excitation component of the discharge-on signal is removed, one can clearly see the two distinct 'peaks' of the component atomic oxygen and dissociative excitation signals at ~20 eV (Noren *et al* 2001b, present work) and ~75 eV (Kanik *et al* 2003), respectively. As D is increased, less of the $S_{\mathrm{O}_2}^{130.4}$ signal is removed, leaving evidence of the dissociative excitation peak in the data (equation (2)). The dissociative excitation peak became distinguishable when D was increased to a value of 0.24 (~10% greater than the quoted value). As D is decreased, more and more of the $S_{\mathrm{O}_2}^{130.4}$ signal is removed. Eventually, a discontinuity in the resulting excitation function develops as the dissociative excitation signal is overweighted. This behaviour was clearly in evidence when D was lowered to 0.20 (~10% less than the quoted value). Therefore, an experimental uncertainty of 10% has been assigned to the dissociation fraction.

Statistical uncertainties in the measurements were essentially dwarfed by the uncertainties discussed previously. Low-energy relative excitation functions had statistical uncertainties between 1 and 3% while those in the high-energy excitation functions were on the order of

1%. Measurements used specifically in the normalization, namely the 100 eV measurements of 130.4 nm discharge-on and -off signals with the 90% O_2/10% N_2 mixture and the relative atomic oxygen signals at each wavelength using the 100% O_2 feed, were all made with statistical uncertainties of 1% or better. All of the individual uncertainties discussed, including those due to polarization effects (discussed in section 3.2), were accumulated in quadrature to arrive at a final estimate of the uncertainty in the experimentally determined cross sections of 24%.

4. Modelling the experimental cross sections

Shemansky and Liu (2003) have constructed a 60-state O I model containing electron reaction parameters in fine structure (i.e. collision strengths are established at the fine structure level). The model, applied here to electron impact on ground state O I, does not represent an *ab initio* theoretical determination of atomic oxygen cross sections. It is, rather, a thorough and simultaneous accounting of the numerous excitations and subsequent emissions resulting from electron impact on a population of ground state oxygen atoms. In modelling the electron–O I reaction, the complex interconnection of various states through branching and cascading channels is specifically taken into account. The model makes use of a detailed library of measured, calculated and inferred excitation and emission cross sections in order to extract direct excitation cross sections for the transitions studied. We specifically point out that the 3p ^{3}P, 4p ^{3}P, 5p ^{3}P, 6p ^{3}P, 4s ^{3}S, (^{2}D^o)3p′ ^{3}D and (^{2}D^o)3p′ ^{3}F states are among the most important states linked through branching and cascade with the measured emissions.

The cross sections in the architecture (i.e. the formatted model of the electronic fine structure) have been adjusted to conform to the measured emission cross sections reported here. This process has required the adjustment of the cross sections in the cascaded components excited mainly by forbidden upward transitions from the ground state. The 3s ^{3}S^o state giving rise to the 130.4 nm transition is affected by more than 20 cascade contributions. The 3d ^{3}D^o state giving rise to the 102.7 nm multiplet contains a dipole allowed branch feeding the 3s ^{3}S^o state in the 1129 nm transition via the 3p ^{3}P state, and also shares cascade components in common with the 3d ^{3}S^o state. The 3s′ ^{3}D^o state producing the 98.9 nm transition also contains a branch feeding the 3s ^{3}S^o state, as does the 3s″ ^{3}P^o state producing the 87.8 nm transition. This interconnection of states and high number of contributors makes it difficult to analyse the small number of measured transitions. A limited measure of confidence in the resulting combination of theoretical and experimentally derived collision strengths is given by the fit of the model to the observed spectrum obtained here at 100 eV impact energy (figure 1). The features labelled 1, 9, 10 and 15 in figure 1, at 87.8, 98.9, 102.7 and 130.4 nm, respectively, are explicitly modelled to fit the corresponding experimental cross sections. We, however, note that the model accurately predicts the 'above-noise' Rydberg series features, labelled 6, 7, 8 and 11 in figure 1, that did not play a role in the adjustment to the experimentally investigated transitions. This provides the confidence that, at least at 100 eV, the model accurately predicts the entire EUV emission spectrum. The calculations of the emission system given here are carried out in exact statistical equilibrium at the fine structure level. The modelled cross sections are calculated analytically using a combination of collision strength Gaussian functions simulating resonance or electron exchange processes in combination with a modified Born approximation (Shemansky and Liu 2003). The modelled cross sections are established on the basis of consistency of the result with the four excitation functions obtained in the present experiment. Theoretical collision strengths for higher states established earlier, contributing to the observed excitation functions, have been modified in order to fit the observed results. The changes required in the theoretical results are described in section 5.

The uncertainty associated with the absolute model cross sections reported here in the electron impact energy region below 100 eV are mainly driven by the basic limitations of

Table 2. Experimental electron-impact-induced emission cross sections for atomic oxygen.

Electron-impact energy (eV)	Cross section ($\times 10^{-18}$ cm^2)			
	130.4 nm	102.7 nm	98.9 nm	87.8 nm
9.51	0.00	—	—	—
10	0.80	—	—	—
11	4.35	—	—	—
12	9.42	—	—	—
12.07	—	0.00	—	—
12.53	—	—	0.00	—
13	14.12	0.74	—	—
14	15.28	1.17	2.18	—
14.11	—	—	—	0.00
15	16.45	1.42	3.48	0.48
16	16.75	1.57	4.28	0.78
18	16.95	1.71	5.16	1.15
20	16.90	1.77	5.65	1.43
25	16.44	1.85	6.42	2.07
30	15.60	1.91	6.81	2.53
35	—	—	—	2.76
40	14.18	1.91	6.95	2.83
50	12.63	1.84	6.93	2.82
75	9.96	1.67	6.55	2.67
100	8.55	1.52	5.88	2.45
200	5.97	1.11	4.51	1.66
300	4.53	0.87	3.58	1.11
400	3.68	0.66	3.02	0.92
500	3.08	0.59	2.48	0.79
750	2.52	0.48	1.86	0.57
1000	2.35	0.50	1.48	0.51

the experimental electron energy-loss measurements, and in the substantial uncertainty in the theoretical physical models of the excitation functions of the higher states of O I close to the ionization limit. The larger uncertainties lie in the near threshold region where atmospheric rate coefficients are mainly determined. At higher energies the accuracy of the cross sections tend to approach the 10% level because of the increasing dominance of the much more accurately known zero-order Born coefficients.

5. Results and discussion

Experimentally determined cross sections have been smoothed and tabulated for convenience in table 2. Plots of the experimental results alongside the data of Zipf and Erdman (1985), Zipf and Kao (1986), Wang and McConkey (1992) and Noren *et al* (2001b) are presented for the O I (130.4 nm), O I (102.7 nm), O I (98.9 nm) and O I (87.8 nm) emission lines in figure 2. The O I (130.4 nm) emission cross sections of Doering and Yang (2001) have not been included here as they are do not represent a direct measurement of the emission cross section. The Doering and Yang (2001) results were derived by summing their direct $2p^4\ ^3P$–$3s\ ^3S^o$ (Doering and Yang 2001) and $2p^4\ ^3P$–$3p\ ^3P$ cross sections (Gulcicek *et al* 1988) along with an estimate of the $3p\ ^3P$ cascade cross section (see Doering and Yang 2001).

Figure 3 shows the experimental data for each of the four measured lines along with the model results for both the emission and direct excitation cross sections. Furthermore,

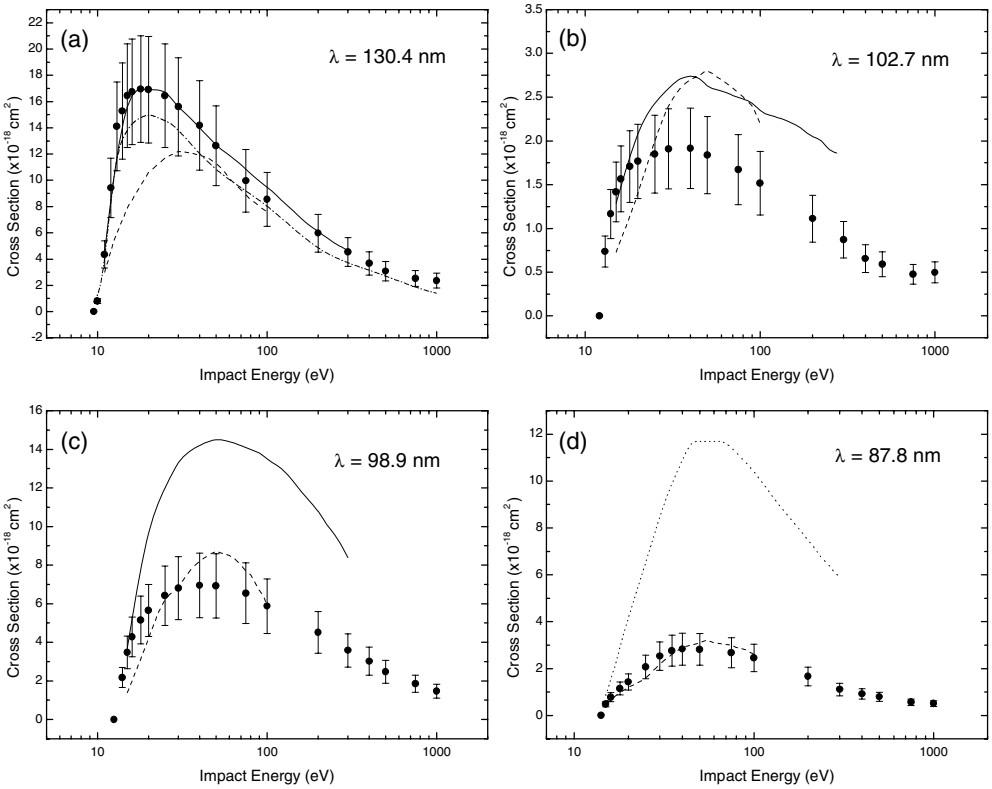

Figure 2. Experimental electron-impact-induced emission cross sections for the $2p^4\ ^3P$–$3s\ ^3S^o$ (130.4 nm), $2p^4\ ^3P$–$3d\ ^3D^o$ (102.7 nm), $2p^4\ ^3P$–$3s'\ ^3D^o$ (98.9 nm) and $2p^4\ ^3P$–$3s''\ ^3P^o$ (87.8 nm) transitions of atomic oxygen. Current results (full circles) are shown alongside the results of Zipf and Erdman (1985) (full curve), Zipf and Kao (1986) (dotted curve), Wang and McConkey (1992) (broken curve) and Noren *et al* (2001b) (chain curve) for comparison.

experimental direct excitation cross sections are included in the figure for comparison. The direct excitation cross sections shown in figure 3 are electron-energy-loss data given by Vaughan and Doering (1987, 1988), Gulcicek and Doering (1988), Doering and Yang (2001) and Kanik *et al* (2001).

Although all cross sections in the model (Shemansky and Liu 2003) are based on analytic coefficients, the emission cross sections can be given only as tabulated quantities because, in general, excitation of a given state involves contributions from a large number of higher levels. A summary of the model results is given in table 3.

5.1. The $2p^4\ ^3P$–$3s\ ^3S^o$ O I (130.4 nm) transition

Figure 2(a) shows that the 130.4 nm excitation function determined in the present work is in good agreement with the Noren *et al* (2001b) results. The shape of the current excitation function is virtually identical to the one presented in Noren *et al* (2001b) with a magnitude approximately 13% larger (well within the combined error limits). However as mentioned in the introduction, the experimental uncertainties have been reduced considerably in the present work from an uncertainty of 34% in the Noren *et al* (2001b) data to a 24% uncertainty quoted in the present work. Remarkable agreement is seen with the Zipf and Erdman (1985) data in

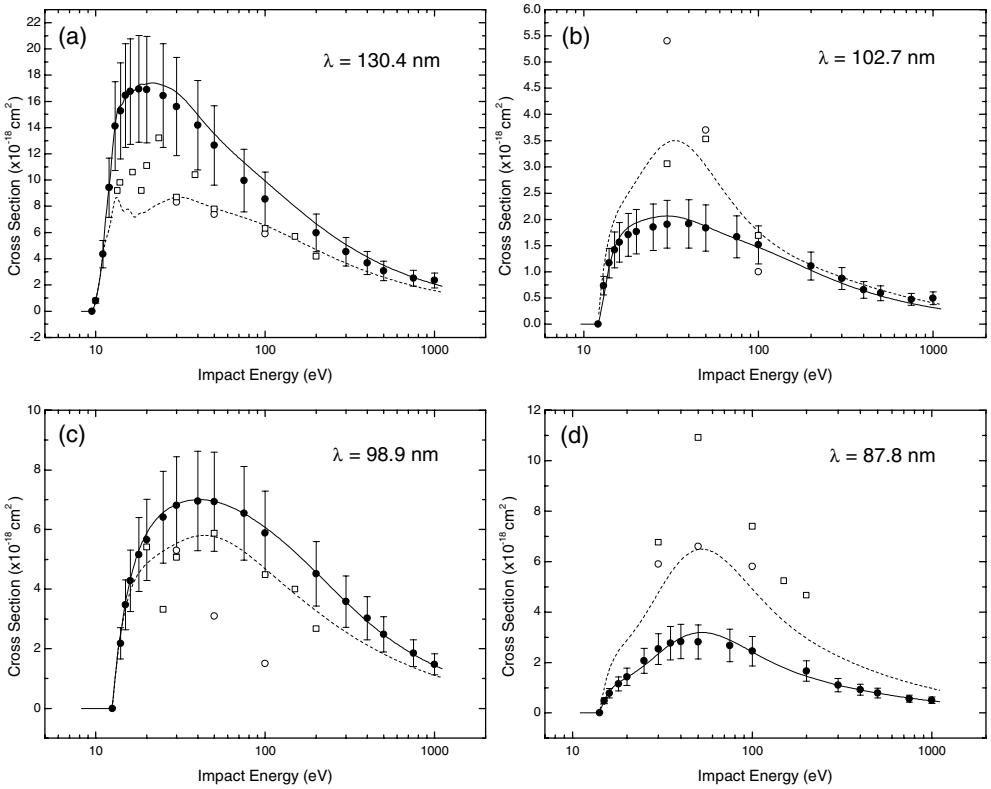

Figure 3. Current experimental (full circles) and model (full curve) emission cross sections for the $2p^4\ ^3P$–$3s\ ^3S^o$ (130.4 nm), $2p^4\ ^3P$–$3d\ ^3D^o$ (102.7 nm), $2p^4\ ^3P$–$3s'\ ^3D^o$ (98.9 nm) and $2p^4\ ^3P$–$3s''\ ^3P^o$ (87.8 nm) transitions of atomic oxygen. Model results for the direct excitation cross sections (broken curve) are also given along with the experimental direct excitation cross sections of Kanik *et al* (2001) (open circles) and those of Doering and co-workers (Vaughan and Doering 1987, 1988, Gulcicek and Doering 1988, Doering and Yang 2001) (open squares).

both shape and magnitude of the excitation function. However, stark differences are seen in the Wang and McConkey (1992) data, which peaks approximately 10 eV higher in energy than the three other excitation functions with a gentler slope rising from threshold. Noren *et al* (2001b) suggested that this may be attributable to an unaccounted for presence of O_2 in the Wang and McConkey (1992) target beam (due to the combination of oxygen atoms). However, as will be discussed in section 5.4, this suggestion appears to be inconsistent with observations of the measured 87.8 nm excitation functions. By comparing the direct excitation cross sections with present results (figure 3(a)) we see that the emission cross sections are significantly larger in the overlapping energy range. This indicates a substantial cascade contribution to the $3s\ ^3S^o$ level.

5.1.1. Model calculations of the $2p^4\ ^3P$–$3s\ ^3S^o$ *O* I *(130.4 nm) transition.* Figure 3(a) shows the excitation and emission cross sections through the application of the modelled O I architecture. The shape of the excitation cross section above 30 eV impact energy is determined by fitting the measured electron energy-loss cross sections obtained by Kanik *et al* (2001) at 30, 50 and 100 eV. At energies above 100 eV, the cross section is forced to conform to the Born approximation zero-order term determined by the known oscillator strength of the electric dipole transition obtained from the current National Institute of Standards and Technology

Table 3. Model results of electron-impact cross sections for atomic oxygen.

Electron-impact energy (eV)	Cross section ($\times 10^{-18}$ cm^2)							
	130.4 nm		102.7 nm		98.9 nm		87.8 nm	
	Em[a]	DE[b]	Em[a]	DE[b]	Em[a]	DE[b]	Em[a]	DE[b]
9	0	0	0	0	0	0	0	0
10	0.85	0.85	0	0	0	0	0	0
11	4.35	4.22	0	0	0	0	0	0
12	9.50	6.32	0	0	0	0	0	0
13	14.21	8.54	0.51	1.06	1.04	1.03	0	0
14	15.68	8.05	1.11	1.66	2.51	2.49	0	0
15	16.46	7.69	1.45	2.00	3.57	3.38	0.51	1.04
16	17.00	7.61	1.65	2.21	4.33	3.94	0.85	1.73
18	17.23	7.43	1.85	2.50	5.31	4.55	1.21	2.46
20	17.33	7.63	1.94	2.74	5.88	4.86	1.41	2.88
22	17.40	7.99	1.99	2.95	6.24	5.06	1.60	3.25
24	17.29	8.24	2.02	3.14	6.48	5.21	1.78	3.64
26	17.13	8.45	2.05	3.29	6.65	5.34	1.98	4.03
28	16.93	8.61	2.06	3.40	6.76	5.45	2.16	4.41
30	16.68	8.69	2.07	3.46	6.85	5.54	2.34	4.77
35	15.84	8.60	2.04	3.49	6.97	5.70	2.72	5.53
40	14.96	8.34	1.99	3.39	7.00	5.79	2.97	6.05
50	13.52	7.87	1.87	3.02	6.95	5.76	3.18	6.48
60	12.48	7.54	1.76	2.65	6.80	5.60	3.14	6.39
75	11.33	7.14	1.63	2.22	6.53	5.25	2.89	5.88
100	9.92	6.53	1.47	1.77	6.07	4.68	2.42	4.92
145	8.13	5.58	1.24	1.37	5.32	3.90	1.84	3.74
195	6.78	4.76	1.05	1.15	4.62	3.32	1.48	3.02
295	5.13	3.70	0.79	0.91	3.61	2.58	1.12	2.28
395	4.17	3.05	0.64	0.76	2.95	2.14	0.92	1.88
495	3.54	2.61	0.55	0.66	2.49	1.84	0.79	1.61
595	3.08	2.29	0.48	0.59	2.17	1.62	0.70	1.42
695	2.74	2.05	0.42	0.53	1.92	1.45	0.63	1.27
795	2.47	1.85	0.38	0.48	1.73	1.31	0.57	1.15
895	2.25	1.70	0.35	0.44	1.58	1.21	0.52	1.06
995	2.08	1.57	0.32	0.41	1.45	1.11	0.48	0.98

[a] Emission cross section.
[b] Direct excitation cross section.

(NIST) database. The fitting process required iterative calculations with the model in order to achieve the experimental relationship between the excitation and emission cross sections. Below 30 eV impact energy it was necessary to include inferred resonance or electron exchange components in order to produce conformity of the model with the experimental measurement of the emission cross section. The inferred structure in the low energy region of the cross section is limited by the energy resolution of the measurements, which is at best $\sim$0.5 eV. Conformity with experiment has forced the scaling-down of the theoretical excitation cross section of the 3p ^{3}P state (Smith 1976) by the factor 0.712. The Tayal and Henry (1989) cross section for the excitation of the 4s ^{3}S state giving rise to the 104.0 nm transition is unchanged in this calculation except for a change in scale to conform to the NIST oscillator strength. The NIST transition probabilities for the 2p^4 ^{3}P–4s ^{3}S^o and 3s ^{3}S^o–4s ^{3}S^o are used in the model to establish the branching to the 3s ^{3}S^o state. The predicted 2p^4 ^{3}P–4s ^{3}S^o (104.0 nm)

emission rate agrees with the observed emission spectrum in figure 1, so these cross sections are entirely consistent with the present experimental results. Cascade contributions to the $3p^4\ ^3P$–$3s\ ^3S^o$ emission from levels higher than the $4s\ ^3S^o$ state are described in the following sections.

5.2. The $2p^4\ ^3P$–$3d\ ^3D^o$ O I (102.7 nm) transition

Both Zipf and Erdman (1985) and Wang and McConkey (1992) give the 102.7 nm excitation function to be approximately 50% larger than the present data (figure 2(b)). Again, the Wang and McConkey (1992) data peak at higher energy than both the Zipf and Erdman (1985) and current excitation functions. The rise from threshold is steeper in the present excitation function than the two other data sets, which display roughly the same slope (albeit differing in magnitude). Figure 3(b) shows that the direct excitation cross sections are considerably larger than the corresponding emission values. This indicates a strong branching channel in the decay of the $3d\ ^3D^o$ state, as discussed below.

5.2.1. Model calculations of the $2p^4\ ^3P$–$3d\ ^3D^o$ O I (102.7 nm) transition. The $3d\ ^3D^o$ state has two emission branches of approximately equal probability, $2p^4\ ^3P$–$3d\ ^3D^o$ (102.7 nm) and $3p\ ^3P$–$3d\ ^3D^o$ (1129 nm). For this reason the direct excitation cross section is actually larger than the emission cross section in the 102.7 nm $2p^4\ ^3P$–$3d\ ^3D^o$ transition (figure 3(b)). The asymptotic limit of the direct excitation cross section is determined by the NIST value of the oscillator strength. It has been necessary to modify the shape and magnitude of the $4p\ ^3P$, $5p\ ^3P$ and $6p\ ^3P$ direct excitation cross sections in order to reproduce the observed $2p^4\ ^3P$–$3d\ ^3D^o$ emission cross section. The electron energy-loss measurements for this transition cannot be used for this analysis because they are contaminated by the nearby $3d\ ^5D^o$ state. The cross section of the $2p^4\ ^3P$–$4p\ ^3P$ direct excitation reaction was calculated by Tayal and Henry (1989). Shemansky and Liu (2003) have scaled the Tayal and Henry (1989) calculations to produce the $5p\ ^3P$ and $6p\ ^3P$ excitation functions. Details of these derived cross sections are given by Shemansky and Liu (2003).

5.3. The $2p^4\ ^3P$–$3s'\ ^3D^o$ O I (98.9 nm) transition

The first note to make regarding the 98.9 nm cross sections is the large discrepancy between the magnitude of the Zipf and Erdman (1985) cross sections and both the Wang and McConkey (1992) and the present cross sections (figure 2(c)). The Zipf and Erdman (1985) values are approximately twice the magnitude of the present results. However, the relative shape of the Zipf and Erdman (1985) excitation function is very similar to that produced in the current investigation. In contrast, Wang and McConkey (1992) give an excitation function that agrees (within uncertainties) in magnitude while showing a distinctly slower rise from threshold and a much more severe drop off as the impact energy increases beyond the peak cross section. All three experimental data sets show peaks around 50 eV, with the Wang and McConkey (1992) data being more sharply peaked than the others. Figure 3(c) indicates a substantial cascade component to the emission cross sections.

5.3.1. Model calculations of the $2p^4\ ^3P$–$3s'\ ^3D^o$ O I (98.9 nm) transition. The dominant loss branch for the $3s'\ ^3D^o$ state is the transition to $2p^4\ ^3P$ (98.9 nm). The cross sections for this transition are determined from the present emission experiment and the electron energy-loss measurements by Kanik *et al* (2001), Gulcicek and Doering (1988), and Vaughan and Doering (1987). The high energy asymptote is determined by the NIST oscillator strength. The cross

section value obtained from Kanik *et al* (2001) at 100 eV is ignored in this analysis because of strong non-conformity with the high energy asymptote. Cascade components from the $(^2D^o)3p'\ ^3D$ and $(^2D^o)3p'\ ^3F$ states are inferred.

5.4. The $2p^4\ ^3P$–$3s''\ ^3P^o$ O I (87.8 nm) transition

The most striking observation regarding the 87.8 nm excitation functions is that the magnitudes of the Zipf and Kao (1986) cross sections are approximately four times larger than the present cross section values at their peak (figure 2(d)). However, the relative shape of the Zipf and Kao (1986) excitation function agrees very well with that produced by the current work. Excellent agreement is seen with the Wang and McConkey (1992) data. This level of agreement indicates that the suggestion put forward by Noren *et al* (2001b), that O_2 was present in the Wang and McConkey (1992) target beam, is not accurate. Spectra taken with the discharge off indicated a substantial cross section for 87.8 nm dissociative excitation of O_2. Therefore, if there were, in fact, an unaccounted-for presence of O_2 in the Wang and McConkey (1992) target beam, then one would not see the level of agreement with the current 87.8 nm cross sections. Direct excitation values lie significantly higher than the present emission cross sections. The $3s''\ ^3P^o$ state is an autoionizing level 0.5 eV above the ionization potential. Furthermore, cascade is not expected to be significant in the 87.8 nm emission, as all higher lying levels are more likely to ionize than to decay to the $3s''\ ^3P^o$ level. Therefore, one expects the direct excitation values to be larger than the emission cross sections. In fact, the ratio of relative contributions to autoionizing and emission channels given by Dehmer *et al* (1977) suggest that the direct excitation cross section should be 2.07 time larger than the emission cross section. This agrees with the current observations within the uncertainties in the quantities involved. Note that this is essentially the same observation and related discussion presented by Wang and McConkey (1992) regarding 87.8 nm emission.

5.4.1. Model calculations of the $2p^4\ ^3P$–$3s''\ ^3P^o$ O I (87.8 nm) transition. The $3s\ ^3P^o$ state, as indicated in section 5.4, is above the ionization limit. There are no inferred cascade transitions. The electron energy-loss measurements (Kanik *et al* 2001), compared with the present emission experiment, indicate an autoionization yield of 57%. The intrinsically more accurate (Dehmer *et al* 1977) measurements provide a yield of 48.3%. We adopt the emission cross section in the present experiment for consistency with the observed emission spectrum. If the Dehmer *et al* (1977) partitioning is accepted, the inferred error in the electron energy-loss experiment is within the experimental uncertainty, as indicated in section 5.4.

6. Conclusions

We have measured and reported experimental electron-impact emission cross sections for the $2p^4\ ^3P$–$3s\ ^3S^o$ (130.4 nm), $2p^4\ ^3P$–$3d\ ^3D^o$ (102.7 nm), $2p^4\ ^3P$–$3s'\ ^3D^o$ (98.9 nm) and $2p^4\ ^3P$–$3s''\ ^3P^o$ (87.8 nm) transitions of atomic oxygen. No consistent trends between the current results and the previously measured emission cross sections were found in regards to agreement/disagreement of either the shape or magnitude of the excitation functions. A high level of agreement is seen between the present data and the cross sections of Zipf and Erdman (1985) at 130.4 nm and those of Wang and McConkey (1992) at 87.8 nm. Noren *et al* (2001b) suggested that the shape of the Wang and McConkey (1992) excitation function was distorted due to an unaccounted-for presence of O_2 in their target beam. However, the present level of agreement between the Wang and McConkey (1992) data at 87.8 nm and those measured at present leads to the conclusion that the Noren *et al* (2001b) assertion is not correct.

Model calculations fitting the experimental measurements have been included, and establish consistency with the NIST oscillator strengths for the electric-dipole-allowed transitions. The experimental results have been found to be consistent with the model for all transitions in the spectral range 85–135 nm, including the Rydberg series ending close to the ionization limit. Application of the model shows that all multiplets reported here have substantial cascade contributions to the emission, with the exception of the 87.8 nm emission from above the first ionization limit. Our requirement for consistency of the model with the presently measured 130.4 nm excitation function implies that the 3p ^{3}P excitation cross section is approximately 70% of the theoretical cross section given by Smith (1976). Excitation functions are presented for each spectral feature from threshold to 1000 eV impact energy.

Acknowledgments

The experimental work present in this paper was carried out at the Jet Propulsion Laboratory and was supported by the NASA Astrophysics and Planetary Atmospheres Program Offices and by NSF Grant ATM-0131210 through a subcontract with the University of Southern California. PVJ gratefully acknowledges financial support from the Research Associateship Program of the National Research Council. The authors also wish to thank J M Ajello for a selfless equipment loan and J W McConkey for his constructive suggestions. The research at the University of Southern California (DES and XL) was supported by NSF Grant ATM-0131210.

References

Abgrall H, Roueff E, Liu X and Shemansky D E 1997 *Astrophys. J.* **481** 557
Abgrall H, Roueff E, Liu X and Shemansky D E 2003 *J. Phys. B: At. Mol. Opt. Phys.* in preparation
Ajello J M, James G K, Franklin B O and Shemansky D E 1989 *Phys. Rev.* A **40** 3524
Dehmer P M, Luken W L and Chupka W A 1977 *J. Chem. Phys.* **67** 196
Doering J P and Yang J 2001 *J. Geophys. Res.* **106** 203
Gulcicek E E and Doering J P 1988 *J. Geophys. Res.* **93** 5879
Gulcicek E E, Doering J P and Vaughan S O 1988 *J. Geophys. Res.* **93** 5885
Heddle D W O 1979 *J. Phys. B: At. Mol. Phys.* **12** 489
Huber K P and Herzberg G 1979 *Molecular Spectra and Molecular Structure: IV Constants of Diatomic Molecules* (New York: Van Nostrand-Reinhold)
Jonin C, Liu X, Ajello J M, Jame G K and Abgrall H 2000 *Astrophys. J.* **129** 247
Kanik I, Johnson P V, Das M B, Khakoo M A and Tayal S S 2001 *J. Phys. B: At. Mol. Opt. Phys.* **34** 2647
Kanik I, Noren C, Makarov O, Ajello J M and McCartney P 2003 *J. Geophys. Res.* at press
Liu X, Ahmed S M, Multari R A, James G K and Ajello J M 1995 *Astrophys. J. Suppl.* **101** 375
Noren C, Kanik I, Ajello J M, McCartney P, Makarov O P, McClintock W E and Drake V A 2001a *Geophys. Res. Lett.* **28** 1379
Noren C, Kanik I, Johnson P V, McCartney P, James G K and Ajello J M 2001b *J. Phys. B: At. Mol. Opt. Phys.* **34** 2667
Shemansky D E, Ajello J M and Hall D T 1985a *Astrophys. J.* **296** 765
Shemansky D E, Ajello J M, Hall D T and Franklin B 1985b *Astrophys. J.* **296** 774
Shemansky D E and Liu X 2003 *J. Geophys. Res.* in preparation
Smith E D R 1976 *Phys. Rev.* A **13** 65
Tayal S S and Henry R J W 1989 *Phys. Rev.* A **39** 4531
Vaughan S O and Doering J P 1987 *J. Geophys. Res.* **92** 7749
Vaughan S O and Doering J P 1988 *J. Geophys. Res.* **93** 289
Wang S and McConkey J W 1992 *J. Phys. B: At. Mol. Opt. Phys.* **25** 5461
Zipf E C and Erdman P W 1985 *J. Geophys. Res.* **90** 11087
Zipf E C and Kao W W 1986 *Chem. Phys. Lett.* **125** 394